# Pressure-tuned many-body phases through Γ-K valleytronics in moiré bilayer $WSe_2$

Brzezińska, Marta; Grytsiuk, Sergii; Rösner, Malte; Gibertini, Marco; Rademaker, Louk

2D Materials



**PAPER** • **OPEN ACCESS**

# Pressure-tuned many-body phases through Γ-K valleytronics in moiré bilayer $WSe_2$

To cite this article: Marta Brzezińska *et al* 2025 *2D Mater.* **12** 015003

2D Materials

PAPER

# Pressure-tuned many-body phases through Γ-K valleytronics in moiré bilayer $WSe_2$

Marta Brzezińska[1], Sergii Grytsiuk[2], Malte Rösner[2], Marco Gibertini[3,4] and Louk Rademaker[5,*]

[1] Institute of Physics, Ecole Polytechnique Fédérale de Lausanne (EPFL), CH-1015 Lausanne, Switzerland
[2] Institute for Molecules and Materials, Radboud University, NL-6525 AJ Nijmegen, The Netherlands
[3] Dipartimento di Scienze Fisiche, Informatiche e Matematiche, University of Modena and Reggio Emilia, IT-41125 Modena, Italy
[4] Centro S3, CNR-NANO Istituto Nanoscienze, IT-41125 Modena, Italy
[5] Department of Quantum Matter Physics, University of Geneva, CH-1211 Geneva, Switzerland
* Author to whom any correspondence should be addressed.

**E-mail:** louk.rademaker@unige.ch

**Keywords:** valleytronics, moiré, bilayer, WSe2, TMDs, pressure, Kondo lattice

Supplementary material for this article is available online

OPEN ACCESS

RECEIVED
18 April 2024

REVISED
28 August 2024

ACCEPTED FOR PUBLICATION
18 September 2024

PUBLISHED
14 October 2024



## Abstract

Recent experiments in twisted bilayer transition-metal dichalcogenides have revealed a variety of strongly correlated phenomena. To theoretically explore their origin, we combine here *ab initio* calculations with correlated model approaches to describe and study many-body effects in twisted bilayer $WSe_2$ under pressure. We find that the interlayer distance is a key factor for the electronic structure, as it tunes the relative energetic positions between the K and the Γ valleys of the valence band maximum of the untwisted bilayer. As a result, applying uniaxial pressure to a twisted bilayer induces a charge-transfer from the K valley to the flat bands in the Γ valley. Upon Wannierizing moiré bands from both valleys, we establish the relevant tight-binding model parameters and calculate the effective interaction strengths using the constrained random phase approximation. With this, we approximate the interacting pressure-doping phase diagram of $WSe_2$ moiré bilayers using self-consistent mean field theory. Our results establish twisted bilayer $WSe_2$ as a platform that allows the direct pressure-tuning of different correlated phases, ranging from Mott insulators, charge-valley-transfer insulators to Kondo lattice-like systems.

## 1. Introduction

Moiré semiconductor heterostructures have proven to be an ideal platform for creating and manipulating nontrivial, correlated electron phases [1]. The observed phenomena range from Mott criticality [2, 3], to Wigner–Mott crystals [4–6], exciton condensation [7] and the quantum anomalous Hall effect [8]. The main constituents in these experiments are moiré bilayers of transition-metal dichalcogenides (TMDs), which come in two forms: heterobilayers, where the two layers are different materials, such as $WSe_2/WS_2$; and homobilayers, where the two layers are the same, such as twisted bilayer $WSe_2$.

Whereas twisted bilayer $WSe_2$ was one of the first materials to reveal correlated insulator physics in transport experiments [9], the correct low-energy description of the relevant flat bands remains a subject of debate. The two main candidates are a Kane–Mele topological insulator model [10, 11] or a triangular Hubbard model [12–15], both derived from states at the K point in the Brillouin zone. The difference between these two flat band models is rooted in the precise symmetries of the moiré potential, which is difficult to estimate from first principles as scanning tunneling microscopy results seem in contradiction with the prevailing density functional theory (DFT) predictions [16]. At the same time, photoemission spectroscopy [17, 18] was not able to resolve the moiré potential and flat bands at the K point, but did observe large moiré gaps and dispersionless bands emerging around the Γ point. Ideally, if one could access the flat bands at the Γ point, it would be possible to realize much stronger electron correlations [19, 20].

In this manuscript, we show how to correctly align predictions from DFT with the experimental observations on twisted bilayer $WSe_2$. Furthermore, we show

that uniaxial pressure can be used to tune the relative energy (and thus occupation) of Γ and K valley states. This, in turn, allows for a plethora of correlated phases: antiferromagnetic insulators and valley-charge-transfer insulators, and their doped counterparts including a Kondo lattice regime. This renders bilayer $WSe_2$ under uniaxial pressure an ideal platform to study correlated metallic states.

In section 2, we use DFT to calculate properties of six differently stacked untwisted bilayer $WSe_2$. These results are used in section 3 to derive the effective flat band physics for both parallel and antiparallel twisted bilayer $WSe_2$. Using estimates for the relevant Coulomb interaction matrix elements based on a Wannierization of the flat bands, we derive a full many-body model and discuss its interacting phase diagram in section 4, revealing distinct correlated and charge-transfer insulators.

## 2. *Ab-initio* results

Monolayer $WSe_2$ has a honeycomb structure with the metal W on one sublattice and two Se on the other sublattice site, vertically displaced in opposite directions with respect to the plane of W atoms. *Untwisted* bilayer $WSe_2$ ($bWSe_2$) can therefore be realized in six different high-symmetry stackings, which are visualized in figure 1(a). Of those, the $2H_{AP}$ is energetically the most stable, followed by the $MX_P$ and $XM_P$ (which are sometimes called 3R stackings) [21]. We performed first-principles calculations using QUANTUM ESPRESSO [22–24] to compute the electronic properties of these differently stacked $bWSe_2$, and how their properties change under applied pressure [25].

Figure 1(b) shows an illustrative band structure of $bWSe_2$. Typically, the valence band maximum is located at K, where the orbital content is predominantly $d_{xy} \pm i d_{x^2-y^2}$ on the W atoms [26]. The bands have a large spin-orbit splitting $\lambda_{SOC}$ originating from the orbital angular momentum at K and K′, and a small interlayer hybridization $w_K$. Additionally, there exists a local valence band maximum at Γ. Here, the orbital content is predominantly $d_{z^2}$, the bands are spin-degenerate but layer-hybridized with interlayer hopping $w_\Gamma$. The energy difference between the Γ and K valley is characterized by the valley offset $\Delta_{\Gamma K}$. In photoemission spectroscopy, $\Delta_{\Gamma K}$ is observed to be about −90 meV, meaning the K valley is higher in energy [18].

We found that the electronic parameters (all energies and splittings at K and Γ, with the exception of the spin–orbit coupling [27]) are extremely sensitive to one specific structural parameter: *the interlayer distance d*, defined as the separation between W planes along the *z*-axis. Other structural parameters, such as the precise locations of the Se atoms and the lattice constant, are subleading [25]. Unfortunately, layered materials such as $bWSe_2$ cannot be correctly described by only (semi)-local functionals, because they do not capture the long-range nature of the interlayer Coulomb and van der Waals (vdW) interactions. An accurate estimation of the interlayer distance *d* from first principles is thus challenging, as it requires either to consider vdW-compliant functional extensions [28] or to resort to more sophisticated—but computationally expensive—approaches such as the Random Phase Approximation (RPA) [29] or Many-Body dispersion [30] methods.

In the specific case of $bWSe_2$, we find that determining an accurate value for *d* is particularly demanding, with an enormous range in predicted interlayer distances, ranging from $d = 6.462$ Å to $d = 7.800$ Å, obtained by relaxing the atomic positions of the $XM_P$ stacking for different pseudopotentials, functionals and vdW corrections (see [25], section IB for details). This, in turn, leads to a range of valley offsets from $\Delta_{\Gamma K} = -89.4$ meV to $-475.3$ meV. The tendency, however, is clear: when the interlayer distance is small, the energy of the Γ valley is higher. Physically, this effect stems from the fact that the interlayer hybridization $w_\Gamma$ of the $d_{z^2}$ orbitals is increased when the interlayer distance is decreased. In contrast, the interlayer hoppings involving $d_{xy}/d_{x^2-y^2}$ orbitals are less affected by the change in interlayer distance (and completely vanish in antiparallel stackings due to spin symmetry). Similarly, we studied how the electronic structure is affected by encapsulating or capping the $WSe_2$ bilayers. Again we found that the interlayer distance *d* is the most significant determinant for $\Delta_{\Gamma K}$, regardless of the environment (see [25], section IC for details).

Although the qualitative tendency under a change of interlayer distance is clear, it does not allow for a quantitative accuracy on energy scales less than roughly 10 meV. For example, a tiny shift in atomic positions of merely 0.01 Å leads to several meV changes in the band energies. Therefore, when we derive moiré flat bands in the next section, we cannot provide exact estimates for the moiré potential. Rather, we describe the tendencies and infer from experiments (such as ARPES [18] or STM [16]) which are the correct DFT predictions. For definiteness, to incorporate vdW corrections in DFT calculations, we employ the rVV10 functional [31, 32], known to reproduce the correct RPA trends for the binding energy of layered materials [33], and that in the specific case of $bWSe_2$ provides lattice parameters and interlayer distances [25] in good agreement with reported RPA results [21].

Since the interlayer distance *d* is the dominant parameter, the most straightforward way to tune the electronic structure is through the application of *uniaxial pressure*. To estimate the interlayer distance as a function of pressure, we fixed various W-W distances in the six high-symmetry bilayer stackings, and relaxed the in-plane lattice constant and other atomic positions. The pressure is extracted

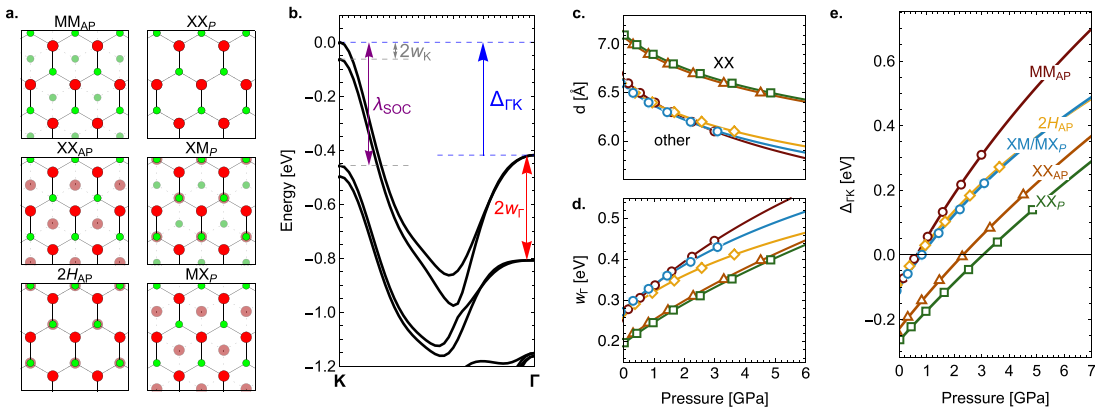


**Figure 1.** (a) Top view of the six possible stacking of untwisted bilayer $WSe_2$. Red corresponds to the W atoms, green to the Se atoms; bright colors are the top layer, faded colors the bottom layer. The three parallel (P) stackings are obtained by starting with the XX stacking and performing a lateral shift of one layer; the three antiparallel (AP) stackings are obtained from the parallel ones by rotating one layer by 180 degrees. Side-views, and a discussion of the stacking naming convention, are given in the supplementary information [25]. (b) The electronic structure of untwisted bilayer $WSe_2$ is characterized by the valence band maxima at Γ and K. Here we show an illustrative band structure for the $XX_P$ stacking, indicating the valley offset $\Delta_{\Gamma K}$, the interlayer splittings $w_{\Gamma/K}$ and the spin–orbit coupling $\lambda_{SOC}$. (c) The interlayer distance $d$, defined as the W-W distance along the $z$-direction, is the dominant physical parameter that determines the electronic structure and can be tuned by applying uniaxial pressure. Here we show the interlayer distance as a function of applied pressure. (d) A decrease in interlayer distance leads to an increase in interlayer hopping $w$ at the Γ-point between W $d_{z^2}$ orbitals. (e) Finally, the application of pressure strongly influences the valley offset $\Delta_{\Gamma K}$. Even though the precise value is hard to predict, here we show the tendency that for different stackings, the $\Delta_{\Gamma K}$ increases with increasing pressure and thus with decreasing interlayer distance $d$.

from *ab initio* calculations using the derivatives of the energy. The resulting distance-pressure curve is shown in figure 1(c), and is consistent with the Murnaghan relation $P = A(e^{-B(1-d/d_0)} - 1)$ with $A, B$ being stacking-dependent parameters [34, 35].

As the interlayer distance decreases with applied pressure, the interlayer hopping between $d_{z^2}$ orbitals increases, as shown in figure 1(d). This, in turn, causes the valence band maximum to shift from the K point to the Γ point, see figure 1(e). Depending on the stacking, the valley transition point happens between $P = 0.5$–$3$ GPa.

## 3. Electronic structure in moiré bilayers

Now that we have analyzed the electronic structure of *untwisted* $bWSe_2$, we will discuss *twisted* $bWSe_2$. This structure exists in two inequivalent forms: so-called parallel or antiparallel stacking, as shown in figures 2(a) and (b). The size of the moiré unit cell depends on the twist angle $\theta$, given in the continuum limit by $a_M = a_{WSe_2}/\sin\theta$. To make a connection between the twisted moiré structures and the untwisted results from previous section, we perform a set of structural relaxations of twisted bilayers using LAMMPS [25, 36]. We look at the angle range $\theta \sim 3$–$6^\circ$ where effects related to lattice reconstruction (such as domain wall network formation) can be neglected [37–39], and which is relevant for the reported transport measurements [9]. Specifically, we consider parallel and antiparallel supercells at angles $\theta = 3.2, 4.4, 5.1, 6.0$ degrees. We quantify the interlayer spacings and bond lengths as a function of the position in the moiré unit cell. Locally, there exists high-symmetry stackings, as shown in figures 2(a) and (b). Interestingly, we found that there is no significant dependence of the in-plane bond lengths $a$ and interlayer distance $d$ on the twist angle $\theta$. Even though the interlayer distance can vary up to 0.3 Å throughout one moiré unit cell, it follows the predicted interlayer distances from the untwisted bilayers: the regions with the largest $d$ correspond to the local XX stacking orders. These results are consistent with [40], further details are presented in the supplementary information [25].

Consequently, we can use the *ab initio* results of the untwisted bilayers of section 2 to predict the electronic structure of twisted bilayers. We follow [10, 41]: the monolayer states at Γ and K are approximated by a parabolic dispersion, and the effect of the twist is captured by the *moiré potential* $\Delta(\mathbf{r})$, which is calculated as follows. Starting with *untwisted* $XX_P$ or $MM_{AP}$ stacking, the other high-symmetry stacks are obtained by performing $s = 0, 1, 2$ shifts of the top layer along the vector $\mathbf{r}_0 = (\mathbf{a}_1 + \mathbf{a}_2)/3$, where $\mathbf{a}_1 = a(1, 0)$ and $\mathbf{a}_2 = a(1/2, \sqrt{3}/2)$. This provides us the sequence of high-symmetry stackings $XX_P \to MX_P \to XM_P$ (or $MM_{AP} \to XX_{AP} \to 2H_{AP}$). In a *twisted* bilayer, the local stacking configuration varies smoothly throughout the moiré unit cell, following the same sequence of stackings. Therefore, the holes in the moiré valence band experience a periodic potential $\Delta(\mathbf{r})$, consistent with the varying energy of the valence band maxima of the untwisted high symmetry stacking. We expand the moiré potential in lowest order of the Fourier expansion over the nearest

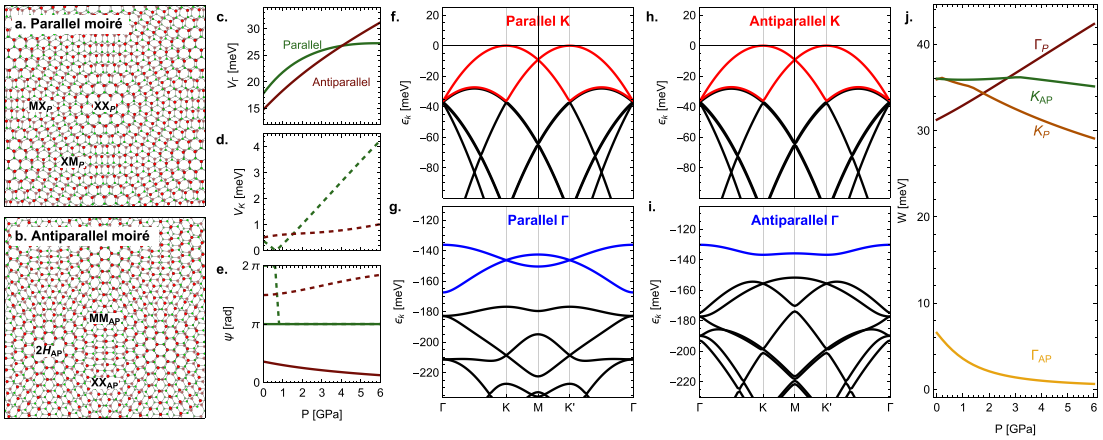


**Figure 2.** (a) The parallel moiré structure, obtained from untwisted $XX_P$ stacking and applying a small twist angle, consists of a hexagonal structure with locally $XX_P$, $XM_P$ and $MX_P$ stacking. Note that the $XM_P$ and $MX_P$ regions are symmetry-related. (b) The antiparallel moiré structure consists of a hexagonal structure with locally $MM_{AP}$, $2H_{AP}$ and $XX_{AP}$ stacking. There is no symmetry relation between the different regions of the moiré unit cell. (c)–(e). By tracing the local valence band maxima at Γ or K at the different stackings in the moiré unit cell, we can extract the moiré potential following equations (1) and (2). Here we show the dependence of the moiré potential amplitude at Γ (c) and K (d) and the moiré potential phase (e) on applied uniaxial pressure. Note that the moiré potential at Γ is an order of magnitude larger than at K. (f) and (g). The electronic band structure of parallel moiré structures at zero uniaxial pressure, throughout the mini-Brillouin zone, for a twist angle $\theta = 3°$. The band structure at K (f) is barely affected by the moiré potential and does not lead to the opening up of significant moiré gaps. On the other hand, there appear isolated moiré flat bands at Γ (g) with honeycomb symmetry, consistent with ARPES observations [18]. (h) and (i). The electronic band structure of antiparallel moiré structures at zero uniaxial pressure, throughout the mini-Brillouin zone, for a twist angle $\theta = 3°$. Similar to the case of parallel moiré structures, the band structure at K (h) shows no signs of moiré gaps. The isolated subset of moiré flat bands at Γ (i) has a triangular lattice symmetry. (j) The bandwidth of moiré flat bands at the top of the Γ and K valley in parallel and antiparallel moiré structures. Most notably are the Γ-states in the antiparallel system, which attain vanishingly small bandwidth under pressure.

moiré reciprocal lattice vectors $\mathbf{g}_j$, $|\mathbf{g}_j| = 2\pi/a$,

$$\Delta(\mathbf{r}) = \sum_{j=1}^{6} V_j \exp\left(i\mathbf{g}_j \cdot \mathbf{r}\right). \tag{1}$$

As $\Delta(\mathbf{r})$ is a real threefold-symmetric function, the values of $V_j$ are constrained, $V_1 = V_3 = V_5, V_2 = V_4 = V_6, V_1 = V_4^* \equiv Ve^{i\psi}$, where $V$ is the real amplitude and $\psi$ is the phase. The values of $V$ and $\psi$ are found by solving the relation

$$E_{(\Gamma,\mathrm{K}),s} = V_0 + 6V\cos\left(\psi + s\cdot\frac{2\pi}{3}\right), \tag{2}$$

for $V_0, V, \psi$, where $E_{(\Gamma,\mathrm{K}),s}$ is the valence band energy at Γ or K given the shift $s$. We calculated the values (amplitude and phase $\psi$) of the moiré potential for both stackings (parallel/antiparallel) and in both valleys (Γ/K) as a function of uniaxial pressure, for a fixed twist angle value $\theta = 3°$.

The calculated moiré potentials shown in figures 2(c)–(e) provide two main results. Firstly, the amplitude of the moiré potential $V$ is an *order of magnitude larger* at Γ than at K. Secondly, pressure increases the potential amplitude $V$. Let us now discuss the details of the moiré electronic structure, for both parallel and antiparallel structures.

In parallel structures, the $XM_P$ and $MX_P$ are symmetry-related through a $2\pi/3$ rotation followed by a layer-flip. Consequently, the moiré potential phase is either $\psi = 0$ or $\pi$. The corresponding moiré flat bands at Γ (using the method of [19, 20]) therefore display a honeycomb symmetry, see figure 2(g). There is a clear gap between the moiré flat bands and the other bands at Γ. By contrast, the moiré potential in the K-valley is very small, leading to the absence of a moiré gap opening, see figure 2(f) (at K, we follow the model of [10]). In real space, the honeycomb structure at Γ is clearly visible in figure 3(b), with localized states at the $XM_P/MX_P$ points of the moiré unit cell. By contrast, the states in the K valley are centered around $XX_P$, see figure 3(d). Note that this is consistent with experimental STM measurements [16]. The small value of the moiré potential and the real-space structure of K valley states we found is consistent with the theoretical work of [12].

A similar pronounced difference between K and Γ valley states is present in antiparallel twisted bilayers. Due to the lack of symmetry between the different local stackings, now there is no constraint on the moiré potential phase. As a result, both Γ and K valley states form a triangular lattice in real space, as shown in figures 3(a) and (c). Because the moiré potential is an order of magnitude larger in the Γ valley, only there we find a well-separated moiré flat band that is spin-degenerate. However, note that due to the absence of interlayer hopping for K valley states in the antiparallel bilayer, the resulting moiré bands are layer degenerate with a spin-layer-valley coupling.

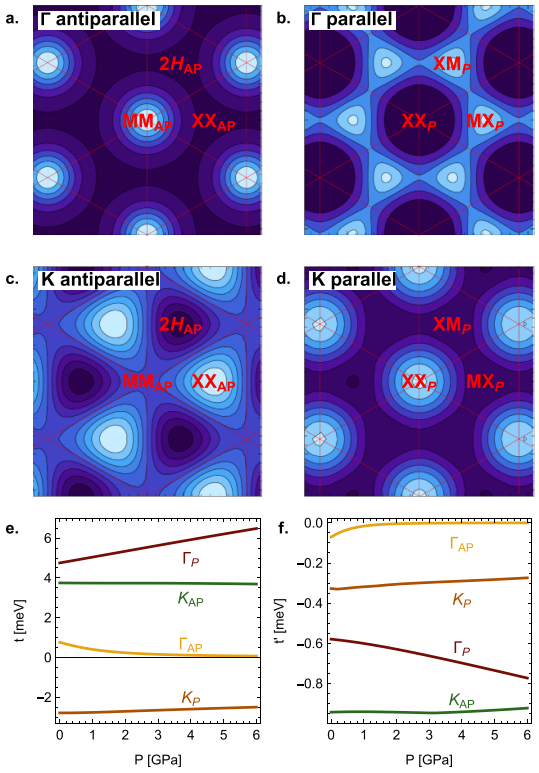


**Figure 3.** (a) Visualization of the Bloch wavefunction in the Γ valley for antiparallel twisted bilayers, shown as the absolute value squared summed over both layers of the wavefunction. Model parameters are $\theta = 3°$ and $P = 0$ GPa. The electronic states is localized in the $MM_{AP}$ region of the moiré unit cell. (b) Same as (a), but for parallel twisted bilayers. We clearly see the emergence of a honeycomb lattice on the $XM_P/MX_P$ positions. (c) Same as (a), but for the K valley states in an antiparallel twisted bilayer. The states are not as localized as in the Γ valley, and are centered around the $XX_{AP}$ position. (d) Same as (c), but for the parallel twisted bilayers. There is less localization compared to the Γ valley, and the states are centered at $XX_{AP}$. (e) and (f) The nearest-neighbor $t$ and next-nearest-neighbor $t'$ tight-binding hopping parameters at $\theta = 3°$ as a function of pressure, for the triangular lattice models relevant for antiparallel twisted bilayers and the K valley of parallel bilayers; as well as for the honeycomb lattice model relevant for the parallel bilayer Γ valley states.

It is interesting to note that the Γ-valley states are, for both parallel and antiparallel stackings, spin-degenerate. On the other hand, due to the spin-valley locking in monolayer $WSe_2$, the K-valley states are also degenerate if we take into account both K and K′ valleys.

Our calculation of the electronic structure in twisted bilayers allows us to compute the effective tight-binding hopping parameters for upmost moiré bands from the two valleys and two stackings. The resulting $t$ and $t'$ as a function of pressure are shown in figures 3(e) and (f). With the exception of the Γ-valley states in parallel stacking, the hopping parameters $t, t'$ decrease with increasing unixial pressure due to the increasing strength of the moiré potential. This exception at $\Gamma_P$ is due to the fact that as the moiré potential increases, the moiré gap at the mini-Brillouin zone K-points increases faster than at Γ, and therefore slightly increases the flat band bandwidth.

Finally, we do not find parameters that put the moiré flat bands in the topological regime, as was originally proposed for twisted bilayer $MoTe_2$ [10]. All effective band structures discussed here are topologically trivial.

## 4. Interacting phase diagram

Up till now we have only discussed band structure effects through the application of pressure in twisted bilayer $WSe_2$. The most striking feature was that the 'flattest' bands exist in the Γ valley, which can be brought to the top of the valence band through pressure. The flatness of these bands prompts us to investigate the effect of interactions. The starting point for this discussion is the Hubbard model of the form

$$H^{vs} = \sum_{\mathbf{k}\sigma} \epsilon^{vs}_{\mathbf{k}\sigma} n_{\mathbf{k}\sigma} + U^{vs} \sum_{i} n_{i\uparrow} n_{i\downarrow} \qquad (3)$$

where $\epsilon^{vs}_{\mathbf{k}\sigma}$ is the non-interacting dispersion in valley $v = \Gamma, \mathrm{K}$ with stacking $s = \mathrm{P}, \mathrm{AP}$. The sites $i$ run over the honeycomb lattice sites at $XM_P/MX_P$ for the parallel stacking Γ states, otherwise they form a triangular lattice. What remains is to find the magnitude of the moiré-scale onsite repulsion $U^{vs}$.

Commonly, the effective Hubbard $U^{vs}$ relevant for the moiré flat bands is derived from the continuum model by constructing a set of continuous Wannier orbitals $w^{vs}_i(\mathbf{r})$ centered at the tight-binding lattice sites $i$, depending on valley $v$ and stacking $s$. Their self-interaction is then $U^{vs}_{ii'} = \int \mathrm{d}^2 r \mathrm{d}^2 r' |w^{vs}_i(\mathbf{r})|^2 V(\mathbf{r} - \mathbf{r}') |w^{vs}_{i'}(\mathbf{r}')|^2$ where $V(\mathbf{r}) = \frac{e^2}{\epsilon}\left[r^{-1} - (r^2 + D^2)^{-1/2}\right]$ is a gate-screened Coulomb interaction with distance to the gate $D$ [41]. However, this neglects all details about the internal screening channels (which enter here only effectively via $\epsilon$ and $D$) and the fact that on the atomic scale the electronic states are not smooth, but in fact are superpositions of $d$-orbitals $\varphi_{j,\alpha}(\mathbf{r})$ on different W atoms labeled by index $j$. The smooth function $w^{vs}_i(\mathbf{r})$ therefore represents the weights on the different atomic $d$ orbitals, so that the *actual* Wannier orbital $\phi^{vs}_i(\mathbf{r})$ becomes

$$\phi^{vs}_i(\mathbf{r}) = \sum_{j \in \{W\}, \alpha} w^{vs}_i(\mathbf{r}_j)\, \varphi_{j,\alpha}(\mathbf{r} - \mathbf{r}_j) \qquad (4)$$

where $j$ sums over all W atoms at positions $\mathbf{r}_j$, and $\alpha$ labels the relevant atomic orbitals, $\alpha = d_{z^2}, d_{x^2-y^2}, d_{xy}$, etc. In order to estimate the Hubbard $U^{vs}$ for the moiré-scale tight-binding model, we thus need to first calculate the relevant $U_{\alpha\beta}$ for the atomic-scale $d$-orbitals of W atoms.

To this end we performed constrained RPA (cRPA) calculations [42] to extract the non-local

Coulomb interactions

$$U_{j\alpha,j'\beta}(R) = \int \mathrm{d}^2 r \mathrm{d}^2 r' |\varphi_{j,\alpha}(\mathbf{r})|^2 U(\mathbf{r}-\mathbf{r}') |\varphi_{j',\beta}(\mathbf{r}'+R)|^2 \quad (5)$$

for the six untwisted bilayer stackings of $WSe_2$ in the atomic $d$ orbital basis. This way, we exclude any screening from the $d$ orbitals, but consistently take the screening from all other states into account. In this case, it turns out that the local stacking details, which change throughout the moiré unit cell and with the twisting angle, do not affect the cRPA screened interactions much (see SI [25] for details), similar to the situation in twisted bilayer graphene [43]. Using the basis transformation from equation (4) we can thus derive the effective moiré $U^{vs}_{\text{moiré}} = \sum_{j,j'} U_{j\alpha,j'\alpha} |w^{vs}(r_j)|^2 |w^{vs}(\mathbf{r}_{j'})|^2$, where $\alpha$ is the relevant $d$-orbital for the given valley and stacking. The twist angle only enters this expression for $U^{vs}$ via the envelope functions $w^{vs}_i(\mathbf{r})$. To this end, we parametrize the onsite cRPA $U_{\alpha\beta}(R)$ with an image-charge model of the form:

$$U(r) = \frac{e}{\varepsilon_m}\left[\frac{1}{\sqrt{r^2+\delta^2}} + 2\sum_{n=1}^{\infty} \frac{1}{\sqrt{r^2+\delta^2+(nh)^2}} \left(\frac{\varepsilon_m - \varepsilon_{\text{env}}}{\varepsilon_m + \varepsilon_{\text{env}}}\right)^n\right], \quad (6)$$

where $e$ is the elementary charge, $h$ represents an effective height of the bilayer, $\delta$ is a parameter allowing to fit the atomic local interaction $U_{ii} = U(r=0)$, $\epsilon_m$ is the effective dielectric constant of the bilayer, and $\epsilon_{\text{env}}$ represents additional screening from the environment, such as substrates as well as all non-Wannierized moiré bands. This is similar to the Keldysh-potential model utilized in [14]. In the supplementary information [25] we show the results of fitting $h$, $\delta$, and $\varepsilon_m$ to *ab initio* cRPA calculations for different pressures, stackings, and for different $d$ orbital channels. We find that the fitting parameters and thus the analytic $U(r)$ model is only mildly affected by pressure and stacking, such that we proceed with using a fixed set of fitting parameters, which are only different for the Γ and K valley models. All together, this provides us with a light-weight effective Hubbard model on the moiré scale, with its model parameters depending on pressure, twist angle, valley (Γ/K) and type of stacking (parallel/antiparallel). For the band structures shown in figure 2 at $\theta = 3°$ twist angle, the relevant interaction parameters for $\epsilon_{\text{env}} = 30$ and $P = 0$ are $U^{\text{K,P}} = 51$ meV, $U^{\Gamma,\text{P}} = 170$ meV, and $U^{\Gamma,\text{AP}} = 132$ meV.

In order to estimate the effect of the Coulomb interactions we performed self-consistent Hartree–Fock mean field theory [25]. As discussed in section 3, the relevant flat bands in antiparallel stackings as well as in the K-valley for parallel stackings form a *triangular* lattice. When $U/t$ is large in the triangular lattice Hubbard model at half-filling, the system becomes a three-sublattice 120° antiferromagnet, which can be qualitatively correctly described by Hartree–Fock theory [44]. Similarly, the effective *honeycomb* lattice Hubbard model relevant for the parallel stacking Γ valley exhibits Néel order for large $U/t$ at half-filling. Note, however, that in terms of doping *per unit cell*, half-filling for a triangular lattice corresponds to $\nu = 1$ whereas half-filling for the honeycomb lattice occurs at $\nu = 2$. Away from half-filling, ferromagnetism is competing with antiferromagnetism [45].

The resulting phase diagrams for parallel and antiparallel stacked moiré bilayers at $\theta = 3°$ degree twist angle in an effective dielectric environment with $\epsilon_{\text{env}} = 30$ are shown in figure 4. Note that the effective $\epsilon_{\text{env}}$ describes both, substrate screening effects as well as screening from all non-Wannierized moiré bands to the Coulomb interaction between electrons within the Wannierized moiré bands. This is why a rather large value is needed here to approximate experimental results, similar as in [12] and [46].

Both diagrams display a prominent valley charge-transfer under the application of pressure. At low hole density ($\nu < 1$ for antiparallel stacking, $\nu < 2$ for parallel stacking) there is a first order transition from states in the K valley to states in the Γ valley.

At half-filling of the Γ valley, we find a pressure-induced transition into an antiferromagnetic charge-transfer insulator. Here the flat bands in the Γ valley are split into the mean-field precursors of lower and upper Hubbard bands. The states of the K valley are now *within the gap* of the Γ valley states. This is exactly the situation described in the Zaanen–Sawatzky–Allen (ZSA) scheme [47], originally intended for cuprates where the oxygen $p$-orbitals are in the gap of the copper $d$-orbitals' lower and upper Hubbard band, which is also referred to as charge-transfer insulating state. When the pressure is further increased, the K states move to lower energy and out of the Γ gap, leading to a regular M–H Ins. of the Γ states.

Upon doping the charge-transfer insulator state, the additional charge carriers occupy the K valley. The resulting situation resembles that of the Kondo lattice model [48, 49], where weakly correlated conduction electrons (from the K valley) coexist with correlated localized electrons (from the Γ valley). In our approximate mean field theory picture, the density of states as presented in figure 5 clearly shows the coexistence of localized and conduction electrons. In the case of the parallel stacking, we also find weak ferromagnetic order in the K valley.

Note that the Kondo lattice regime occurs in parallel stacking at hole densities $\nu = 2 + \delta$, whereas in

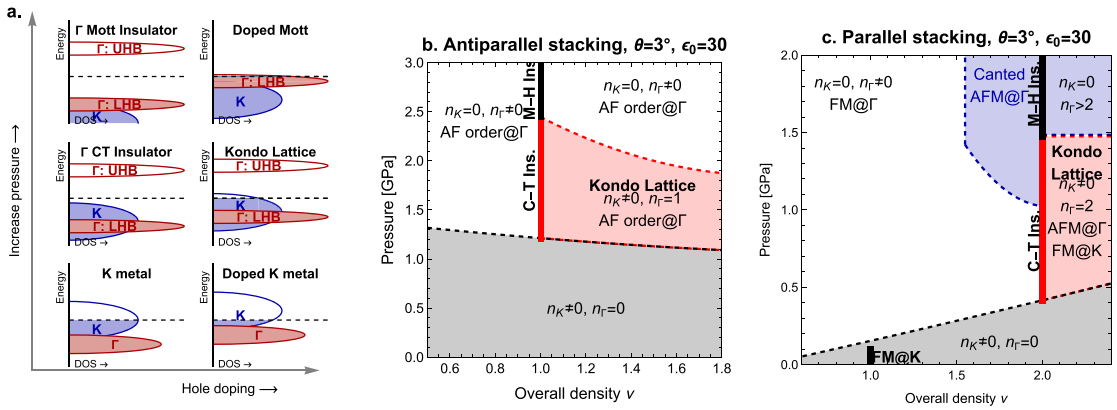


**Figure 4.** (a) Qualitatively, we can already identify various many-body phases that are expected in tbWSe$_2$ under pressure. Here, we visualize six possible phases by plotting a cartoon density of states versus energy. At zero or low pressure, the charge carriers will fill up states in the weakly correlated K valley (bottom row), leading to metallic behavior. At half-filling (left column), an increase in pressure leads to a charge-transfer to the strongly correlated Γ valley. The Γ states will split into a lower and upper Hubbard band (LHB/UHB), yielding an insulator state. Depending on the position of the remaining K valley states, this is a charge-transfer (CT) insulator at intermediate pressures, or a Mott–Hubbard insulator at high pressures. Increasing the hole doping beyond half-filling (right column) now yields either a Kondo lattice model at intermediate pressures, or a doped Mott insulator at high pressures (b) and (c) The qualitative picture is confirmed by numerical mean field theory calculations. Here we show the resulting phase diagram for antiparallel (b) and parallel (c) stacking at twist angle $\theta = 3^\circ$ and dielectric constant $\epsilon_0 = 30$, as a function of hole density $\nu$ and pressure $P$. We confirm that at a critical pressure the electronic charge is fully shifted from the K to the Γ valley. At half-filling of the Γ valley states ($\nu = 1$ for antiparallel stacking, $\nu = 2$ for parallel stacking), applying pressure induces a transition from a conducting K state to an antiferromagnetic Γ charge-transfer insulator (C-T Ins.), followed by a transition to a Mott–Hubbard insulator (M–H Ins.). Increasing the hole density $\nu$ in the charge-transfer insulator leads to a Kondo lattice regime, with localized electrons in the Γ valley and conduction electrons in the K valley.

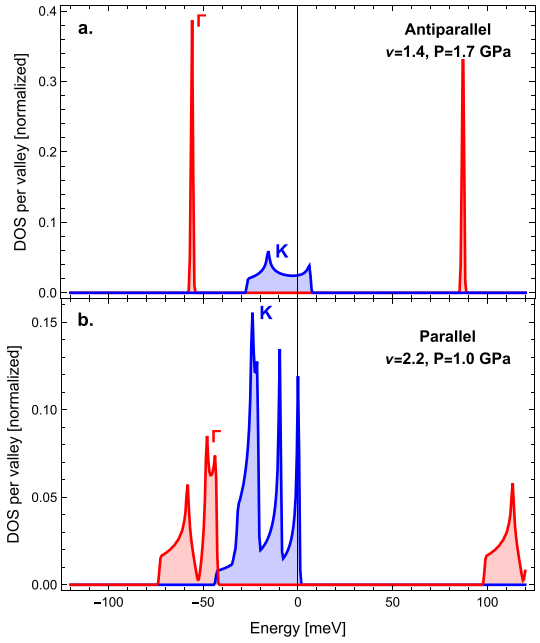


**Figure 5.** The density of states in the Kondo lattice regime of the phase diagrams of figure 4, for antiparallel (a) and parallel (b) stacking. In both cases the strong correlations of the Γ states at half-filling lead to the formation of lower and upper Hubbard bands. Upon doping away from half-filling, the Fermi level ($E = 0$) crosses the K valley states that are lying within the gap of the Γ states. The result is a system with localized electrons in the Γ valley and conduction electrons in the K valley.

the antiparallel bilayers it occurs at densities $\nu = 1 + \delta$. This difference arises because in the parallel stacking, the states in the Γ valley realize a honeycomb lattice, which requires a hole density $\nu = 2$ per unit cell become Mott insulating. On the other hand, the Γ valley states in the antiparallel stacking realize a triangular lattice, requiring $\nu = 1$ for Mott localization.

The mean field phase diagram consists thus of a wealth of different correlated phases: at half-filling both types of ZSA insulators, and away from half-filling either doped Mott insulator or Kondo lattice systems. These correlated metallic phases are ill-understood, and likely show a richer behavior than can be inferred from naive mean field theory. However, by identifying where twisted bilayer WSe$_2$ hosts these different correlated conducting phases we pave the way for further *quantitative* studies that compare theories and experiments.

## 5. Outlook

In summary, we have found that the dominant structural parameter of bilayer WSe$_2$ is the interlayer distance $d$, as it affects the relative energy of the Γ and K valley states. Consequently, in twisted bilayer WSe$_2$ the effective strength of the interaction—which is much higher in the Γ valley than in the K valley—can be tuned through uniaxial pressure. The resulting valley charge-transfer allows for a multitude of interesting correlated phases.

Recently, the idea of using pressure to induce a valley shift in (twisted) bilayer TMDs has been addressed in two other theoretical publications [50, 51] and their *ab initio* results are consistent with our findings in section 2. However, they do not discuss

the strength nor the effect of many-body Coulomb interactions. At the other extreme, a recent work [35] suggesting a fractional Chern insulator in pressurized twisted bilayer WSe2 ignores the valley degree of freedom. Our results bridge this gap and presents the whole picture as we have explored the full interplay between valley charge transfer and correlation effects.

Note that the valley degree of freedom can also be tuned using a perpendicular electric field [52, 53]. The states at the Γ valley are more sensitive than K valley states to an applied electric field, as they correspond to orbitals that are more extended in the $z$-direction. However, we find tuning by electric field to be less feasible for a twisted bilayer, as a perpendicular electric field also couples to the layer degree of freedom. The interlayer distance can also be tuned by chemical intercalation, as already shown experimentally [54]. Also in this case, changing the chemical composition might induce further changes to the electronic structure, and as such we expect pressure to be the 'cleanest' way to induce a valley shift.

Experimentally, applying pressure on moiré bilayers is shown to be feasible using diamond anvil cells. This initially started with pressure-studies in twisted bilayer graphene [55] and twisted double bilayer graphene [56]. Recently, a hydrostatic pressure experiment was performed on twisted bilayer $WSe_2$ [57]. Using exciton photoluminescence [58], they showed that indeed the energy of the Γ valley was shifted upwards, which is consistent with our predictions. A natural next step would be to perform transport experiments in the spirit of the [9], revealing new correlated insulator states under pressure. We note in passing that the relevant pressure to reveal valleytronic effects is of the order of a few GPa, depending on the filling and type of stacking. This is a one order of magnitude smaller than the pressure required to close the band-gap of $WSe_2$ [59] (in the range 28–62 GPa) or related TMD systems [60, 61].

Among our predicted phases is a Kondo lattice regime with localized electrons in the Γ valley and conduction electrons in the K valley. Similar Kondo lattice physics, but in terms of the *layer* degree of freedom (instead of the *valley* suggested in our work), has been observed in twisted $WSe_2$ homobilayers [62] and $MoTe_2/WSe_2$ heterobilayers [63]. The properties of the Kondo lattice many-body phase will strongly depend on the interactions and possible hybridization between the localized and conduction states—as such it would be interesting to quantitatively compare the layer-Kondo lattice to the valley-Kondo lattice regime, and to traditional heavy fermion systems [49, 64] and the 'topological' heavy fermions proposed for twisted bilayer graphene [65, 66] or trilayer graphene [67]. Such a comparison, from a theoretical side, would require to go beyond the simple mean-field theory picture presented here. Strong correlation methods are needed, such as Dynamical Mean Field Theory [68], which recently has been used to study TMD moiré bilayers [14, 15] as well as other flat band materials [65, 66, 69]. In addition, a more precise modeling of the inter-valley couplings is required, as well as possible emerging interactions such as the RKKY coupling between the localized electrons. Another aspect that pushes beyond our current model is the appearance of strong longer-ranged Coulomb interactions in the Γ valley, that can stabilize fractionalized [70] or generalized Wigner crystal phases [4, 46]. In any case, such theoretical explorations should be fueled by new experiments on twisted bilayer $WSe_2$ under pressure.

## Data availability statement

All data that support the findings of this study are included within the article (and any supplementary files).

## Acknowledgments

We acknowledge discussions with Abhay Pasupathy and the late Jan Zaanen. L R was funded by the SNSF via Starting Grant TMSGI2_211296. M R acknowledges support from the Dutch Research Council (NWO) via the 'TOPCORE' consortium and from the research program 'Materials for the Quantum Age' (QuMat) for financial support. The latter program (registration number 024.005.006) is part of the Gravitation program financed by the Dutch Ministry of Education, Culture and Science (OCW). M G acknowledges financial support from the Italian Ministry for University and Research through the PNRR Project ECS_00000033_ECOSISTER and the PRIN2022 project 'Simultaneous electrical control of spin and valley polarization in van der Waals magnetic materials' (SECSY). The computations were performed at the Swiss National Supercomputing Centre (CSCS) under Project No. s1146 and at the Dutch National Supercomputer Snellius under Project No. EINF-4184.

## ORCID iDs

Marta Brzezińska https://orcid.org/0000-0003-0657-4382
Sergii Grytsiuk https://orcid.org/0000-0003-0499-6944
Malte Rösner https://orcid.org/0000-0002-6199-2176
Marco Gibertini https://orcid.org/0000-0003-3980-5319
Louk Rademaker https://orcid.org/0000-0001-6053-8150

## References

[1] Mak K F and Shan J 2022 Semiconductor moiré materials *Nat. Nanotechnol.* **17** 686

[2] Ghiotto A *et al* 2021 Quantum criticality in twisted transition metal dichalcogenides *Nature* **597** 345
[3] Li T *et al* 2021 Continuous Mott transition in semiconductor moiré superlattices *Nature* **597** 350
[4] Regan E C *et al* 2020 Mott and generalized Wigner crystal states in WSe2/WS2 moiré superlattices *Nature* **579** 359
[5] Jin C *et al* 2021 Stripe phases in WSe2/WS2 moiré superlattices *Nat. Mater.* **20** 940
[6] Tang Y *et al* 2023 Evidence of frustrated magnetic interactions in a Wigner–Mott insulator *Nat. Nanotechnol.* **18** 233
[7] Wang Z, Rhodes D A, Watanabe K, Taniguchi T, Hone J C, Shan J and Mak K F 2019 Evidence of high-temperature exciton condensation in two-dimensional atomic double layers *Nature* **574** 76
[8] Li T *et al* 2021 Quantum anomalous hall effect from intertwined moiré bands *Nature* **600** 641
[9] Wang L *et al* 2020 Correlated electronic phases in twisted bilayer transition metal dichalcogenides *Nat. Mater.* **19** 1
[10] Wu F, Lovorn T, Tutuc E, Martin I and MacDonald A H 2019 Topological insulators in twisted transition metal dichalcogenide homobilayers *Phys. Rev. Lett.* **122** 086402
[11] Devakul T, Crépel V, Zhang Y and Fu L 2021 Magic in twisted transition metal dichalcogenide bilayers *Nat. Commun.* **12** 6730
[12] Pan H, Wu F and Sarma S D 2020 Band topology, Hubbard model, Heisenberg model and Dzyaloshinskii-Moriya interaction in twisted bilayer WSe2 *Phys. Rev. Res.* **2** 033087
[13] Zang J, Wang J, Cano J and Millis A J 2021 Hartree-Fock study of the moiré Hubbard model for twisted bilayer transition metal dichalcogenides *Phys. Rev.* B **104** 075150
[14] Ryee S and Wehling T O 2023 Switching between Mott-Hubbard and Hund physics in Moiré quantum simulators *Nano Lett.* **23** 573
[15] Tscheppe P *et al* 2024 Magnetism and metallicity in moiré transition metal dichalcogenides *Proc. Natl Acad. Sci.* **121** e2311486121
[16] Zhang Z, Wang Y, Watanabe K, Taniguchi T, Ueno K, Tutuc E and LeRoy B J 2020 Flat bands in twisted bilayer transition metal dichalcogenides *Nat. Phys.* **16** 1093
[17] Pei D *et al* 2022 Observation of Γ-Valley Moiré bands and emergent hexagonal lattice in twisted transition metal dichalcogenides *Phys. Rev.* X **12** 021065
[18] Gatti G *et al* 2023 Flat Γ Moiré bands in twisted bilayer WSe2 *Phys. Rev. Lett.* **131** 046401
[19] Zhang Y, Liu T and Fu L 2021 Electronic structures, charge transfer and charge order in twisted transition metal dichalcogenide bilayers *Phys. Rev.* B **103** 155142
[20] Angeli M and MacDonald A H 2021 Γ valley transition metal dichalcogenide moiré bands *Proc. Natl Acad. Sci.* **118** e2021826118
[21] He J, Hummer K and Franchini C 2014 Stacking effects on the electronic and optical properties of bilayer transition metal dichalcogenides MoS2, MoSe2, WS2 and WSe2 *Phys. Rev.* B **89** 075409
[22] Giannozzi P *et al* 2009 QUANTUM ESPRESSO: a modular and open-source software project for quantum simulations of materials *J. Phys.: Condens. Matter* **21** 395502
[23] Giannozzi P *et al* 2017 Advanced capabilities for materials modelling with Quantum ESPRESSO *J. Phys.: Condens. Matter* **29** 465901
[24] Giannozzi P *et al* 2020 Quantum ESPRESSO toward the exascale *J. Chem. Phys.* **152** 154105
[25] See Online supplementary information.
[26] Liu G-B, Shan W-Y, Yao Y, Yao W and Xiao D 2013 Three-band tight-binding model for monolayers of group-VIB transition metal dichalcogenides *Phys. Rev.* B **88** 085433
[27] Jafari H, Barts E, Przybysz P, Tenzin K, Kowalczyk P J, Dabrowski P and Sławińska J 2024 Robust Zeeman-type band splitting in sliding ferroelectrics *Phys. Rev. Mater.* **8** 024005
[28] Klimes J and Michaelides A 2012 Perspective: Advances and challenges in treating van der Waals dispersion forces in density functional theory *J. Chem. Phys.* **137** 120901
[29] Lu D, Li Y, Rocca D and Galli G 2009 Ab initio Calculation of van der Waals Bonded Molecular Crystals *Phys. Rev. Lett.* **102** 206411
[30] Tkatchenko A, DiStasio R A, Car R and Scheffler M 2012 Accurate and efficient method for many-body van der Waals interactions *Phys. Rev. Lett.* **108** 236402
[31] Vydrov O A and Van Voorhis T 2010 Nonlocal van der Waals density functional: the simpler the better *J. Chem. Phys.* **133** 244103
[32] Sabatini R, Gorni T and Gironcoli S D 2013 Nonlocal van der Waals density functional made simple and efficient *Phys. Rev.* B **87** 041108
[33] Björkman T, Gulans A, Krasheninnikov A V and Nieminen R M 2012 van der Waals bonding in layered compounds from advanced density-functional first-principles calculations *Phys. Rev. Lett.* **108** 235502
[34] Carr S, Fang S, Jarillo-Herrero P and Kaxiras E 2018 Pressure dependence of the magic twist angle in graphene superlattices *Phys. Rev.* B **98** 085144
[35] Morales-Durán N, Wang J, Schleder G R, Angeli M, Zhu Z, Kaxiras E, Repellin C and Cano J 2023 Pressure-enhanced fractional Chern insulators along a magic line in moiré transition metal dichalcogenides *Phys. Rev. Res.* **5** L032022
[36] Thompson A P *et al* 2022 LAMMPS - a flexible simulation tool for particle-based materials modeling at the atomic, meso and continuum scales *Comput. Phys. Commun.* **271** 108171
[37] Weston A *et al* 2020 Atomic reconstruction in twisted bilayers of transition metal dichalcogenides *Nat. Nanotechnol.* **15** 592
[38] Enaldiev V V, Zólyomi V, Yelgel C, Magorrian S J and Fal'ko V I 2020 Stacking domains and dislocation networks in marginally twisted bilayers of transition metal dichalcogenides *Phys. Rev. Lett.* **124** 206101
[39] Nielsen C E M, da Cruz M, Torche A and Bester G 2023 Accurate force-field methodology capturing atomic reconstructions in transition metal dichalcogenide moiré system *Phys. Rev.* B **108** 045402
[40] Vitale V, Atalar K, Mostofi A A and Lischner J 2021 Flat band properties of twisted transition metal dichalcogenide homo- and heterobilayers of $MoS_2$, $MoSe_2$, $WS_2$ and $WSe_2$ *2D Mater.* **8** 045010
[41] Wu F, Lovorn T, Tutuc E and MacDonald A H 2018 Hubbard model physics in transition metal dichalcogenide Moiré Bands *Phys. Rev. Lett.* **121** 026402
[42] Aryasetiawan F, Imada M, Georges A, Kotliar G, Biermann S and Lichtenstein A I 2004 Frequency-dependent local interactions and low-energy effective models from electronic structure calculations *Phys. Rev.* B **70** 195104
[43] Westerhout T, Katsnelson M I and Rösner M 2021 Quantum dot-like plasmonic modes in twisted bilayer graphene supercells *2D Mater.* **9** 014004
[44] Szasz A, Motruk J, Zaletel M P and Moore J E 2020 Chiral spin liquid phase of the triangular lattice Hubbard model: a density matrix renormalization group study *Phys. Rev.* X **10** 021042
[45] Hirsch J E 1985 Two-dimensional Hubbard model: numerical simulation study *Phys. Rev.* B **31** 4403
[46] Tan Y, Tsang P K H, Dobrosavljević V and Rademaker L 2023 Doping a Wigner-Mott insulator: Exotic charge orders in transition metal dichalcogenide moiré heterobilayers *Phys. Rev. Res.* **5** 043190
[47] Zaanen J, Sawatzky G A and Allen J W 1985 Band gaps and electronic structure of transition-metal compounds *Phys. Rev. Lett.* **55** 418
[48] Coleman P 2015 *Introduction to Many-Body Physics* (Cambridge University Press)

[49] Rademaker L and Mydosh J 2016 Chapter 280 quantum critical matter and phase transitions in rare earths and actinides *Handbook Phys. Chem. Rare Earths* **49** 293
[50] Gao Y, Xu Q, Farooq M U, Xian L and Huang L 2023 Switching the Moiré lattice models in the twisted bilayer $WSe_2$ by strain or pressure *Nano Lett.* **23** 7921
[51] Olin S, Jmukhadze E, MacDonald A H and Lee W-C 2023 Ab-initio study of the energy competition between Γ and K valleys in bilayer transition metal dichalcogenides (arXiv:2310.17824)
[52] Huang D and Kaxiras E 2016 Electric field tuning of band offsets in transition metal dichalcogenides *Phys. Rev.* B **94** 241303
[53] Ramasubramaniam A, Naveh D and Towe E 2011 Tunable band gaps in bilayer transition-metal dichalcogenides *Phys. Rev.* B **84** 205325
[54] Ding Y *et al* 2021 Bidirectional and reversible tuning of the interlayer spacing of two-dimensional materials *Nat. Commun.* **12** 5886
[55] Yankowitz M, Chen S, Polshyn H, Zhang Y, Watanabe K, Taniguchi T, Graf D, Young A F and Dean C R 2019 Tuning superconductivity in twisted bilayer graphene *Science* **363** 1059
[56] Szentpéteri B *et al* 2021 Tailoring the band structure of twisted double bilayer graphene with pressure *Nano Lett.* **21** 8777
[57] Xie X, Ding J, Wu B, Zheng H, Li S, Wang C-T, He J, Liu Z, Wang J-T and Liu Y 2023 Pressure-induced dynamic tuning of interlayer coupling in twisted $WSe_2/WSe_2$ homobilayers *Nano Lett.* **23** 8833
[58] Mak K F, Xiao D and Shan J 2018 Light–valley interactions in 2D semiconductors *Nat. Photon.* **12** 451
[59] Wang X, Chen X, Zhou Y, Park C, An C, Zhou Y, Zhang R, Gu C, Yang W and Yang Z 2017 Pressure-induced iso-structural phase transition and metallization in $WSe_2$ *Sci. Rep.* **7** 46694
[60] Zhao Z *et al* 2015 Pressure induced metallization with absence of structural transition in layered molybdenum diselenide *Nat. Commun.* **6** 7312
[61] Zhou Y *et al* 2018 Pressure-induced metallization and robust superconductivity in pristine 1T-$SnSe_2$ *Adv. Electron. Mater.* **4** 1800155
[62] Xu Y, Kang K, Watanabe K, Taniguchi T, Mak K F and Shan J 2022 A tunable bilayer Hubbard model in twisted $WSe_2$ *Nat. Nanotechnol.* **17** 934–9
[63] Zhao W, Shen B, Tao Z, Han Z, Kang K, Watanabe K, Taniguchi T, Mak K F and Shan J 2023 Gate-tunable heavy fermions in a moiré Kondo lattice *Nature* **616** 61
[64] Si Q and Steglich F 2010 Heavy fermions and quantum phase transitions *Science* **329** 1161
[65] Datta A, Calderón M J, Camjayi A and Bascones E 2023 Heavy quasiparticles and cascades without symmetry breaking in twisted bilayer graphene *Nat. Commun.* **14** 5036
[66] Rai G, Crippa L, Călugăru D, Hu H, Medici L D, Georges A, Bernevig B A, Valentí R, Sangiovanni G and Wehling T 2023 Dynamical correlations and order in magic-angle twisted bilayer graphene (arXiv:2309.08529)
[67] Ramires A and Lado J L 2021 Emulating heavy fermions in twisted trilayer graphene *Phys. Rev. Lett.* **127** 026401
[68] Georges A, Kotliar G, Krauth W and Rozenberg M J 1996 Dynamical mean-field theory of strongly correlated fermion systems and the limit of infinite dimensions *Rev. Mod. Phys.* **68** 13
[69] Crippa L, Bae H, Wunderlich P, Mazin I I, Yan B, Sangiovanni G, Wehling T and Valentí R 2024 Heavy fermions vs doped Mott physics in heterogeneous Ta-dichalcogenide bilayers *Nat. Commun.* **15** 1357
[70] Cai J *et al* 2023 Signatures of fractional quantum anomalous Hall states in twisted $MoTe_2$ *Nature* **622** 63